Graphene bentonite supported ZnFe₂O₄ as superparamagnetic photocatalyst for antibiotic degradation

Pardeep Singh[1], Sourav Gautam[1], Pooja Shandilya[1], Bhanu Priya[1], Virender P. Singh[2], Pankaj Raizada[1]

[1]*School of Chemistry, Shoolini University of Biotechnology and Management Sciences, Solan -173212, Himachal Pradesh, India*
[2]*School of Physics, Shoolini University of Biotechnology and Management Sciences, Solan -173212, Himachal Pradesh, India*

*Corresponding Author, Tel: (+91) 1792-308000, (+91) 9459316882; Fax: +91-1792-30800;
Email: pardeepchem@gmail.com

Abstract

The supported photocatalysis is emerging as an effective technology to overcome of inherent drawbacks of bare magnetic photocatalysts. Herein, $ZnFe_2O_4$ was immobilized over graphene sand composite (GSC) and bentonite (BT) to report $ZnFe_2O_4$/GSC and $ZnFe_2O_4$/BT photocatalyst. The size of $ZnFe_2O_4$/GSC and $ZnFe_2O_4$/BT was obtained as 100 and 50 nm, respectively. Both photocatalysts exhibited band gap of 1.95 eV. $ZnFe_2O_4$/GSC and $ZnFe_2O_4$/BT had BET surface area of 15.6 and 14.5 cm^2, respectively. The appearance of D and G band in Raman spectra indicated the formation of graphene sand composites. The superparamagnetic property of photocatalyst resulted in quick separation photocatalyst form reaction solution. The adsorption and photocatalytic capability of $ZnFe_2O_4$/GSC and $ZnFe_2O_4$/BT was evaluated for photo-mineralization of ampicillin and oxytetracycline antibiotics. The adsorption process showed significant effect on mineralization of selected antibiotics. Simultaneous adsorption and degradation (A+P) process was highly effective for antibiotic degradation. More than 90% of antibiotic mineralization was obtained in 10 hours. The power law model authorized the complex nature of degradation process. Magnetically recoverable photocatalyst exhibited significant recycling efficiency due to easier recovery of photocatalysts. Copyright © 2017 VBRI Press.

Keywords: Superparamagnetic $ZnFe_2O_4$, supported-photocatalysis, antibiotic mineralization, kinetics.

Introduction

Antibiotics are the most widely prescribed medicines which find their way into aquatic system. Non-biodegradable and persistent antibiotics are regarded major threat to the quality of water resources [1]. In this context, various remedial methods such as adsorption chemical oxidation, ozone treatment, coagulation, flocculation, and reverse osmosis have been used to eliminate antibiotics form water resources [2]. However, these methods do not result in complete removal or produce large volume of secondary level pollutants [2].

During last two decades, semiconductor mediated photocatalysis is regarded as fast growing wastewater technology. The environmentalists are more focused on designing of novel visible light photocatalysts with high activity, recyclability and stability in aqueous medium. Very recently, ferrites (MFe_2O_4, M= Fe, Zn, Co, Ni etc.) have emerged as potential materials with extensive use in electronic devices [3], information storage [4], magnetic resonance imaging [5], drug-delivery technology [6] and semiconductor photocatalysis [7–9]. Particularly, zinc ferrite ($ZnFe_2O_4$) is a narrow bandgap semiconductor with a band-gap (1.8-2.0)eV and thus have better visible-light-responsive photocatalytic nature [10, 11]. Many efforts have been made recently for the desirable fabrications of $ZnFe_2O_4$ nanostructures with diverse morphologies such as nano tubes [7, 12], nanorods [8, 13], nanofibers [14, 15], micro-/nanospheres [10, 16] and hollow spheres [17, 18]. However, agglomeration of magnetic nanoferrites hinder large scale applicability of ferrites for waste water treatment [19]. Moreover, initial adsorption of pollutant from water is highly needed for effective surface facilitated photo-degradation remedial process [20]. These concerns have resulted in development of new class of photocatalytic systems involving the immobilization

of metal oxides onto a solid support such as activated carbon, carbon nanotubes and biopolymers. Recently, graphene and its derivatives have received great consideration due to various interesting property. These materials have capability to delocalize electrons, generate free radical and have long term stability [21]. Graphene has layered sp^2 hybridized carbon arranged in two dimensional [22]. Hu *et al.* reported the synthesis of graphene/ZnS nanocomposite using microwave radiation based process [23]. Liu *et al.* synthesized BiOI/GSC composite using hydrothermal method and observed higher stability and enhanced photocatalytic efficiency for methylene green degradation [24].

Bentonite clay is another attractive support materials for nanoparticles owing to its low price, availability and environmental friendly nature [25]. Bentonite (montmorillonite) is a phyllosilicate mineral with two tetrahedral sheets sandwiching on octahedral sheet. Bentonite has a permanent negative charge due to the isomorphous substitution of Al^{3+} for Si^{4+} in the tetrahedral site and Mg^{2+} for Al^{3+} in the octahedral site [26]. Bentonite possesses excellent adsorption/ion exchange sites for metal ions and organic pollutants within its interlayer space [27]. Recent studies have highlighted good substrate nature of bentonite for designing of photocatalytic system. For instance, ZnS/bentonite [28], TiO_2/bentonite [29], CdS/bentonite [30], g-C_3N_4/bentonite [31], $BiVO_4$/bentonite [32] etc. were previously synthesized and tested for their improved photocatalytic activity.

In precedent work, superparamagnetic $ZnFe_2O_4$ was supported on graphene and bentonite to overcome the inherent drawbacks of unsupported $ZnFe_2O_4$. The presence of graphene and bentonite resulted in lower agglomeration of $ZnFe_2O_4$ in reaction solution. Secondly, both graphene and bentonite had sufficient adsorption capacity for antibiotics to make the effective surface photocatalytic degradation reaction. The non-toxic and highly carbonaceous sucrose was used as a precursor to prepare graphene sand composite (GSC). The simple and economical synthetic method was adopted to prepare GSC [33]. The sand was used prevent the agglomeration of graphene sheets. Power law model was used to study mineralization kinetics. The prepared nanocomposites were characterized by using various spectral techniques. The photocatalytic efficiency of GSC/$ZnFe_2O_4$ and $ZnFe_2O_4$/BT was explored photodegradation of ampicillin and oxytetracycline antibiotic. The recycle efficiency of $ZnFe_2O_4$/GSC and $ZnFe_2O_4$/BT was also testified for ten catalytic cycles to verify the effectiveness of prepared photocatalysts.

Experimental

Synthesis of graphene sand composite (GSC)

The graphene sand composite (GSC) was prepared with modification in method reported by Thalappil and co-workers [33]. Briefly, 50 mg of sugar was dissolved in 200 mL of water. To this solution, 20 mg of sand was added and mixture stirred for 24 hours to black thick slurry. The sugar encapsulated sand was heated at 550 °C for 3 hour to attain complete graphitization of sugar molecules. Finally, obtained GSC was preserved for further use.

Preparation of ZnFe$_2$O$_4$/GSC and ZnFe$_2$O$_4$/BT

$ZnFe_2O_4$/GSC was prepared with modification in work by Feng and co-workers [34]. The different solutions of $Fe(NO_3)_3 \cdot 9H_2O$ (0.1 N in 50 mL), $NaBH_4$ (0.2 N in 25 mL) and $Zn(NO_3)_2 \cdot 6H_2O$ (0.1 N in 50 mL) were prepared in deionized water. To $Fe(NO_3)_3 \cdot 9H_2O$ solution, $NaBH_4$ was added dropwise with continuous stirring. Now 2 mg of GSC was added and solution was stirred for 30 min. To the resultant mixture, $Zn(NO_3)_2 \cdot 6H_2O$ was added with continuous stirring for 1 hour followed by heating at 80 °C for 8 h to form $ZnFe_2O_4$/GSC. The obtained $ZnFe_2O_4$/GSC precipitates were washed and dried at 100°C. $ZnFe_2O_4$/BT was prepared using above mentioned procedure by using bentonite in place of GSC. $ZnFe_2O_4$ was prepared by same methodology with no inclusion of GSC or BT.

Photocatalytic activity

The adsorptional and photocatalytic activity of $ZnFe_2O_4$/GSC and $ZnFe_2O$/BT was explored using double walled pyrex vessel (ht. 7.5 cm x dia.6 cm) having thermostatic water circulation arrangement (30 ± 5°C). The antibiotic solution containing photocatalyst suspension was exposed to solar irradiation. The absorbance of ampicillin and oxytetracycline in supernatant liquid was recorded at 260 and 350 nm, respectively. The solar light intensity was monitored by digital lux-meter. The chemical oxygen demand (COD) and CO_2 measurements were measured using previously reported methods [35]. The inorganic ions were analyzed using total dissolved solid (TDS) meter. The removal efficiency was calculated using Eq. 1:

$$\% \text{ removal effciency} = \frac{C_0 - C_t}{C_0} \qquad (1)$$

where, C_0 is the initial concentration of antibiotics and C_t is instant concentration of antibiotics in test solution. During recycling experiment, photocatalyst was separated from reaction using external magnetic field. The supernatant liquid was persevered for analysis. The separated photocatalysts were washed with water and used for subsequent efficiency experiment. The pH drift method was used to find pH of zero-point charge(pH_{pzc}) [35].

Characterization techniques

FESEM micrographs of prepared photocatalysts were obtained using Nava Nano SEM-45(USA) and sample surfaces. HR-TEM and energy dispersive X-ray analysis were conducted using   FP/5022 -

Tecnai G2 20 S-TWIN (USA) under vacuum. The Perkin– Elmer Spectrometer (Spectrum RX-I) was used to obtain FTIR spectra. FTIR absorption spectra were recorded in the region of 400–4000 cm^{-1}. Panalytical's X'Pert Prodiffractrometer was used for powder XRD analysis to identify the presence of different phases and crystallinity in the sample. The diffuse reflectance spectrophotometer (UV 3600, Shimadzu) was used to investigate the optical absorption performance of photocatalysts using BaSO$_4$ as reference for analysis. The magnetic studies were undertaken using vibrating sample magnetometer (VSM) (Cryogenic). Raman analysis was using FT-Raman spectrometer (BRUKEF RFS 27: standalone with range of 50-4000 cm^{-1} using 2 cm^{-1} resolutions). Brunauer–Emmett–Teller (BET) analysis was performed using Autosorb I; Quatachrome Corp. to measure the specific surface.

Results and Discussion

Characterization of ZnFe$_2$O$_4$/GSC and ZnFe$_2$O$_4$/BT

Fig. 1(a, b) shows FESEM pictures of GSC and BT, respectively. Graphene sand composite and bentonite have rough surface with different pore size for better attachment of photocatalyst over its surface and adsorption of antibiotics **[36]**. The FESEM images in (**Fig. 1(c, d)**) represents stacking of ZnFe$_2$O$_4$ to graphene sand and bentonite respectively. The FESEM images clearly indicated the attachment of ZnFe$_2$O$_4$ over GSC and bentonite. XRD patterns of ZnFe$_2$O$_4$/GSC, ZnFe$_2$O$_4$/BT, ZnFe$_2$O$_4$, GSC and BT are shown in (**Fig. 1(e-f)**. The peak at 26.63° was due to plane (002) of graphene **[37] (Fig. 1-e1).** The characteristic broad peak at 26.37° was attributed to plane (003) for bentonite molecule **(JCPDS 03-0019) (Fig. 1-f1)**. The diffraction peaks of ZnFe$_2$O$_4$ at 29$\colon$89°, 35$\colon$37°, 42$\colon$85°, 51$\colon$11°, 56$\colon$76° and 62$\colon$13° were assigned to (2 2 0), (3 1 1), (4 0 0), (4 2 2), (5 1 1), and (4 4 0) **(Fig. 1-e2 and f2)**. All these peaks indicated cubic phase of spinel zinc ferrite **(JCPDS No. 74-2397)**. The major characteristic diffraction peaks of ZnFe$_2$O$_4$ in both ZnFe$_2$O$_4$/BT and ZnFe$_2$O$_4$/GSC at 2θ value of 29.2°, 35.1°, 41.84°, 50.31°, 56.5°, and 62.24° can be indexed to (220), (311), (400), (422), (511) and (440) crystal plane, respectively **(Fig.1e(3) and 1f(3))**. In case of ZnFe$_2$O$_4$/GSC and ZnFe$_2$O$_4$/BT, characteristic peaks of ZnFe$_2$O$_4$, GSC and BT were observed in XRD spectra of composites. The intensity of diffraction peaks in ZnFe$_2$O$_4$, GSC and BT was decreased in ZnFe$_2$O$_4$/GSC and ZnFe$_2$O$_4$/BT. The reduction in intensity of diffraction peaks was due to interaction between ZnFe$_2$O$_4$ and GSC /BT.

The TEM pictures of ZnFe$_2$O$_4$/GSC and ZnFe$_2$O$_4$/BT are depicted in **(Supplementary Fig. S1)**. The dispersion of ZnFe$_2$O$_4$ aggregates was clearly seen over bentonite and GSC **(S1 c-d)**. Magnified images indicated clear stacking of ZnFe$_2$O$_4$ with graphene sand composite and bentonite. The size of ZnFe$_2$O$_4$/GSC and

ZnFe$_2$O$_4$/BT was obtained as 100 and 50 nm, respectively. SAED pattern of both ZnFe$_2$O$_4$/GSC and ZnFe$_2$O$_4$/BT indicated semi crystalline nature of prepared photocatalysts **(S1 e-f)**.

EDX pattern of GSC, BT, ZnFe$_2$O$_4$/GSC and ZnFe$_2$O$_4$/BT was recorded for elemental analysis. In GSC, presence of P, Si, C, Cl and O designated the covering of graphene over sand (**Supplementary Fig. S2a**).

The presence of Si, P and Cl was mainly due to presence SiO$_2$, PO$_3^{4-}$ and Cl$^-$ ions in sand. Bentonite was mainly composed of K, Na, Ca and Al elements (**Supplementary Fig. S2b**). ZnFe$_2$O$_4$/GSC indicated a clear presence of Zn, Fe, C, Si, P, Cl and O in sample (**Supplementary Fig. S2c**). The presence of Zn, Fe, Si, Na and O confirmed the formation of ZnFe$_2$O$_4$/BT (**Supplementary Fig. S2d**). FTIR spectra of GSC, BT, ZnFe$_2$O$_4$/GSC and ZnFe$_2$O$_4$/BT are revealed in (**Supplementary Fig. S2e**). In GSC spectrum, the characteristics peaks at 1941 and 1632 cm^{-1} were due to C =O stretching of COOH groups and C–O–C stretching vibrations, respectively. The peaks 1080 cm^{-1} was due to stretching vibration of C=C bond **[38, 39, 40]**.
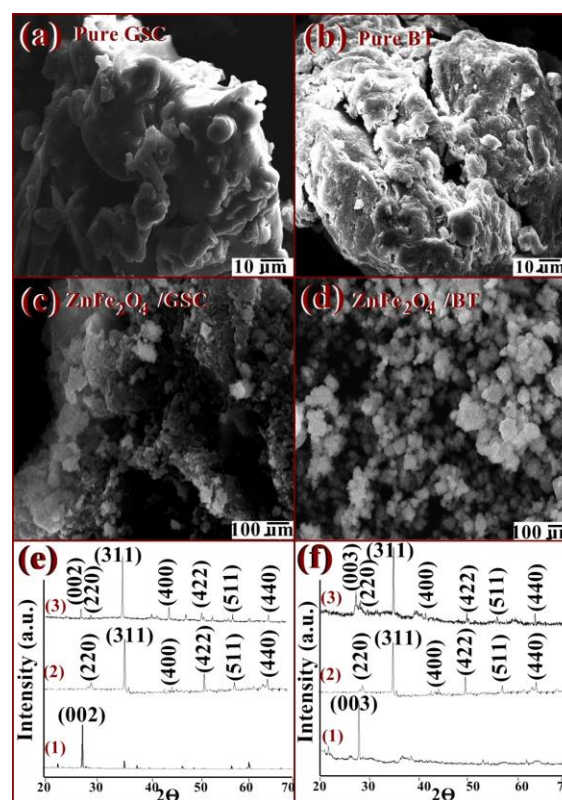

Fig. 1. (a) FESEM picture of GSC, (b) FESEM picture of native BT, (c) FESEM image of ZnFe2O4/GSC, (d) FESEM images of ZnFe2O4/BT, (e) XRD spectra of (1) GSC, (2) ZnFe2O4, (3) ZnFe2O4/GSC and (f) XRD spectra of (1) BT, (2) ZnFe2O4 (3) ZnFe2O4/BT.

The band appearing at 472 cm^{-1} was due to the SiO$_2$ group present in river sand **[41]**. The band at 2931 cm^{-1} was ascribed to C-H stretching of sucrose and the peak at 3410 cm^{-1} was emerged due to O–H stretching vibration or adsorption of water molecules onto GSC **[36]**. The peaks at 778 cm^{-1} was assigned

Fig. 2. (a-d) BET analysis and Raman spectra of $ZnFe_2O_4$/GSC and $ZnFe_2O_4$/BT. Raman spectra of (c) $ZnFe_2O_4$/GSC and GSC (d) $ZnFe_2O_4$/BT and BT.
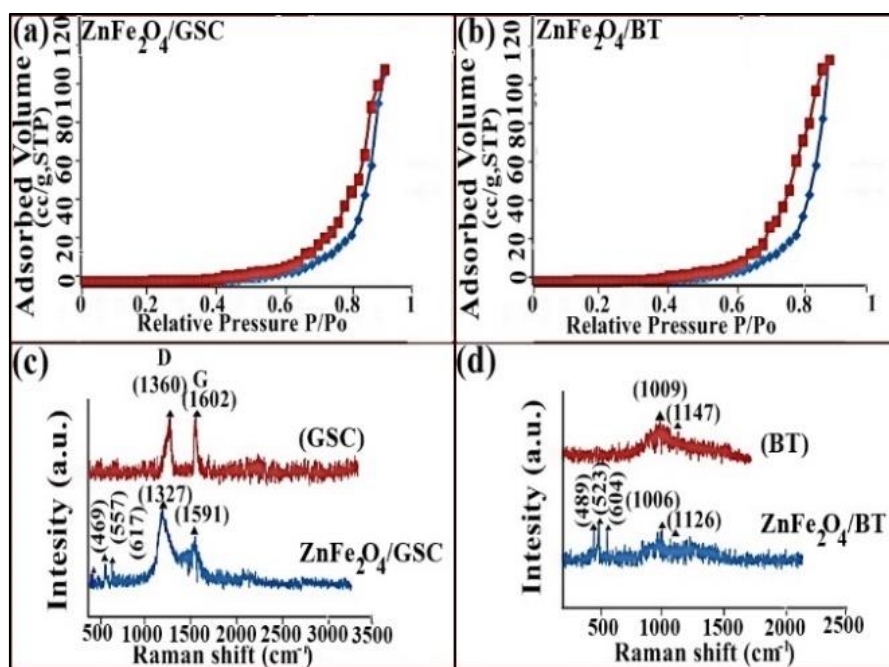
to Si-O stretching mode **[42]**. In case of $ZnFe_2O_4$/GSC, the peak at 574 and 436 cm^{-1} was due to Zn-O and Fe-O stretching vibrations, respectively **[43]**. The formation of $ZnFe_2O_4$/GSC nanocomposite was confirmed by alteration of peaks of GSC towards lower wave number (3410 to 3391, 1632 to 1630, 1080 to 1042 and 778 to 703 cm^{-1}). In case of bentonite, peaks at 3678 and 679 cm^{-1} were credited to Al-OH-Mg and Si-O-Mg bonds respectively **[44]**. The peaks at 3431 and 1636 cm^{-1} were related to OH frequencies of the water molecule **[45]**. The band at 914 cm^{-1} were typical of dioctahedral smectites and band at 795 cm^{-1} due to presence of quartz in the bentonite **[46]**. The peak at 1032cm^{-1} corresponding to Si-O stretching **[47]**. The peaks at 572 and 440 cm^{-1} in $ZnFe_2O_4$/BT was due to Zn-O and Fe-O stretching vibrations, respectively **[43]**. The alteration in peaks from 3678 to 3671, 3431 to 3430, 1636 to 1634, 1032 to 1030, 914 to 901, 795 to 793 and 679 to 668 cm^{-1} confirmed the interaction between BT and $ZnFe_2O_4$.

BET adsorption experiments were carried out to observe the porosity in $ZnFe_2O_4$/ GSC and $ZnFe_2O_4$/ BT. **Fig. 2a and b** displays N_2 adsorption/desorption isotherm and pore size distribution of $ZnFe_2O_4$/ GSC and $ZnFe_2O_4$/ BT. The isotherm type IV isotherm which reveals the mesoporous nature of $ZnFe_2O_4$/ GSC and $ZnFe_2O_4$/ BT **[48]**. The most of the pore is less than 20 nm. The specific surface area of $ZnFe_2O_4$/GSC and $ZnFe_2O_4$/BT are 15.6 and 14.5 cm^2, respectively.

Fig. 2c and d show Raman spectra of $ZnFe_2O_4$/GSC, $ZnFe_2O_4$/BT, GSC and BT. In case of GSC, two peaks were observed at 1360 cm^{-1}(D) and 1602 cm^{-1}(G). The G band was ascribed to E_{2g} phonon of sp^2 bonded carbon **[49]**. The D band was due to local defects and disorders present in graphene. In the Raman spectra of $ZnFe_2O_4$/GSC, peak at 469, 557 and 617cm^{-1} was assigned to the $ZnFe_2O_4$ nanoparticles **(Fig. 2c)**. The other two dominant peaks at 1327 and 1591 cm^{-1} were assigned to D and G band of graphene **[50]**. However, no such bands were observed in Raman spectra of bentonite. In case of bentonite the characteristics peaks were noticed at 1009 and 1147 cm^{-1} **(Fig. 2d)**. Thses peaks were due to distortation of SiO_4 tertahetra from T_d symmtery to C_{3v} symmtery **[51]**. In Raman spectra of $ZnFe_2O_4$/BT, peak at 489, 523 and 604 cm^{-1} was assigned to $ZnFe_2O_4$ nanoparticles, while peaks at 1006 and 1126 cm^{-1} were due to the presence of bentonite in $ZnFe_2O_4$/BT.

From application point of view, it is important that photocatalyst/adsorbents should possess paramagnetic nature to realize fast separation under external applied magnetic field. **Fig. 3** displays the magnetization of $ZnFe_2O_4$/GSC and $ZnFe_2O_4$/BT with respect to applied magnetic field. Both $ZnFe_2O_4$/GSC and $ZnFe_2O_4$/BT possessed saturation magnetization (M_s) values of 12.36 emu/gm and 12.86 emu/gm. The obtained values are quite low as compared to reported M_s values of $ZnFe_2O_4$ in literature (45.9 emu/gm) **[52]**. The lower M_s value were attributed to the existence of non-magnetic GSC and bentonite present in $ZnFe_2O_4$/GSC and $ZnFe_2O_4$/BT. The coercivity value (H_c) for $ZnFe_2O_4$/GSC and $ZnFe_2O_4$/BT was found to be zero. The hysteresis loop (M-H curve) showed the superparamagnetic behavior of prepared photocatalyst **(Fig. 3a and c)**. These obtained magnetic properties are sufficient for quick magnetic separation under external magnetic field **(Fig. 3b and d)**. The photocatalysts were separated in 30 secs using external magnetic field. $ZnFe_2O_4$, $ZnFe_2O_4$/GSC and $ZnFe_2O_4$/BT were used as

adsorbent/photocatalyst during antibiotic mineralization from aqueous solution. After photocatalytic/adsorption experiment, the photocatalyst can be separated from reaction mixture in 30 sec by placing a permanent magnet near sample bottle. Both ZnFe$_2$O$_4$/GSC and ZnFe$_2$O$_4$/BT can be used as magnetic photocatalyst during photodegradation of antibiotics.
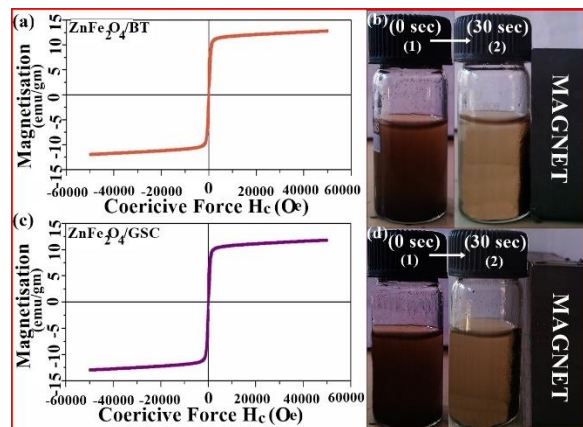

Fig. 3. (a-d) The magnetization hysteresis loop and magnetic separation of ZnFe$_2$O$_4$/BT and ZnFe$_2$O$_4$/GSC. (a) Hysteresis loop of ZnFe$_2$O$_4$/BT, (b) Magnetic separation of ZnFe$_2$O$_4$/BT. (c) Hysteresis loop of ZnFe$_2$O$_4$/GSC, (d) Magnetic separation of ZnFe$_2$O$_4$/GSC (1) in the absence of magnetic field (2) under external magnetic field.

UV-visible diffuse reflectance analysis was performed to find the band gap of prepared photocatalysts (**Supplementary Fig. S3**). ZnFe$_2$O$_4$, ZnFe$_2$O$_4$/GSC and ZnFe$_2$O$_4$/BT exhibited absorption at 420 nm. The band gap analysis was,

$$\alpha h\upsilon = B\left(h\upsilon - E_g\right)^n \qquad (2)$$

where, α = absorption coefficient = 2.303 A/l, hυ indicates photon energy, B belongs to band tailoring. The optical band gap is determined by extrapolating the straight portion of curve between $(\alpha h\upsilon)^2$ and hυ when α = 0. The respective band gap of ZnFe$_2$O$_4$/GSC and ZnFe$_2$O$_4$/BT was found to be 1.95 eV. In present study, pH$_{zpc}$ of ZnFe$_2$O$_4$/GSC and ZnFe$_2$O$_4$/BT was found to be 5.9 and 5.7, respectively (**Supplementary Fig. S4**).

AMP and OTC degradation using different catalytic systems

The catalytic efficiency of ZnFe$_2$O$_4$/GSC and ZnFe$_2$O$_4$/BT was tested for the removal of ampicillin and oxytetracycline antibiotics present in aqueous phase. **Table 1** illustrates AMP and OTC removal using various catalytic systems. The removal of AMP and OTC from aqueous phase through direct photolysis had negligible effect on antibiotic. However, the decrease in OTC and AMP concentration was significant in the presence of ZnFe$_2$O$_4$/GSC and ZnFe$_2$O$_4$/BT under solar light. During 60 min exposure to solar light, 95%, 85%, 62%, 36% and 27 % of removal efficiency was

attained using ZnFe$_2$O$_4$/GSC, ZnFe$_2$O$_4$/BT, ZnFe$_2$O$_4$, GSC and BT, respectively. However, in the absence of solar light ZnFe$_2$O$_4$/GSC, ZnFe$_2$O$_4$/BT, ZnFe$_2$O$_4$, GSC and BT displayed 36%, 31%, 27%, 25%, and 23 % of AMP removal from reaction medium (**Table 1**). Under solar light, 98 % and 91% of OTC was degraded using ZnFe$_2$O$_4$/GSC and ZnFe$_2$O$_4$/BT, respectively (**Table 1**). During adsorption process, 41% and 32% of OTC was removed using ZnFe$_2$O$_4$/GSC and ZnFe$_2$O$_4$/BT, respectively. Efficiency trend of adsorbents was observed as ZnFe$_2$O$_4$/GSC >ZnFe$_2$O$_4$/BT > ZnFe$_2$O$_4$ > GSC > BT. These results indicate that photocatalytic evaluation of both ZnFe$_2$O$_4$/GSC and ZnFe$_2$O$_4$/BT was quite different from binary or ternary inorganic metal oxide photocatalyst. The adsorption capacity of photocatalyst has as critical role during surface photodegradation reaction.

Table 1. Removal of AMP and OTC using ZnFe2O4/BT and ZnFe2O4/GSC. (a) photocatalytic removal of AMP, (b) adsorption of AMP, (c) photocatalytic removal of OTC and (d) adsorption of OTC: Reaction condition [AMP]= 1 × 10-4mol dm-3 ; [OTC] = 1 × 10-4 mol dm-3 ; [catalyst] = 50 mg/100 ml; pH= 6.0; time = 60 min(AMP) and 120 min (OTC); Solar light intensity = 35 x 103± 1000 lx.

Catalytic system	% AMP removal		% OTC removal	
	Under solar light	In Dark	Under solar light	In Dark
ZnFe$_2$O$_4$/GSC	95	36	98	41
ZnFe$_2$O$_4$/BT	85	31	91	32
ZnFe$_2$O$_4$	62	27	51	23
GSC	36	25	29	12
BT	27	23	20	8

Adsorption behavior of ZnFe$_2$O$_4$/GSC and ZnFe$_2$O$_4$/BT

The amount of antibiotics adsorbed onto ZnFe$_2$O$_4$/GSC and ZnFe$_2$O$_4$/BT at time t (min) was calculated using following equation [53, 54]:

$$q_e = (C_o - C_e)\frac{V}{M} \qquad (3)$$

where, q_e (mg g^{-1}) denotes antibiotics adsorbed per gram of adsorbent at time t(min). C_0 and C_t indicate initial and final concentration of antibiotics (dm^{-3}) is the concentration of AMP/OTC (mol dm^{-3}) at time t(min). V is the volume of the reaction solution (50 ml) and m is the mass of the adsorbent (g). The pseudo first order rate is given by Eq. **4 [53, 54]**:

$$(q_e - q_t) = log\, q_e - \frac{k_1\, t}{2.303} \qquad (4)$$

where, q_t is absorbed antibiotics (mg/g) in time t. A plot of log (q_e-q_t) *versus* t provides a linear relationship. k_1 and q_e were determined from the slope and intercept. The pseudo second order rate expression can be expressed by **Eq. 5 and 6 [53, 54]**:

Fig. 4(a-b). The removal of antibiotics using ZnFe₂O₄/GSC, ZnFe₂O₄/BT and ZnFe₂O₄ under different reaction conditions. Reaction condition: [AMP] = 1x10⁻⁴mol dm⁻³; [OTC]= 1x10⁻⁴mol dm⁻³; [catalyst] = 50 mg/100ml ; pH= 6.0;   Solar light intensity= 35 x 10³± 1000 lx; reaction time = 60 min for adsorption and A+P and 120 min for A-P.
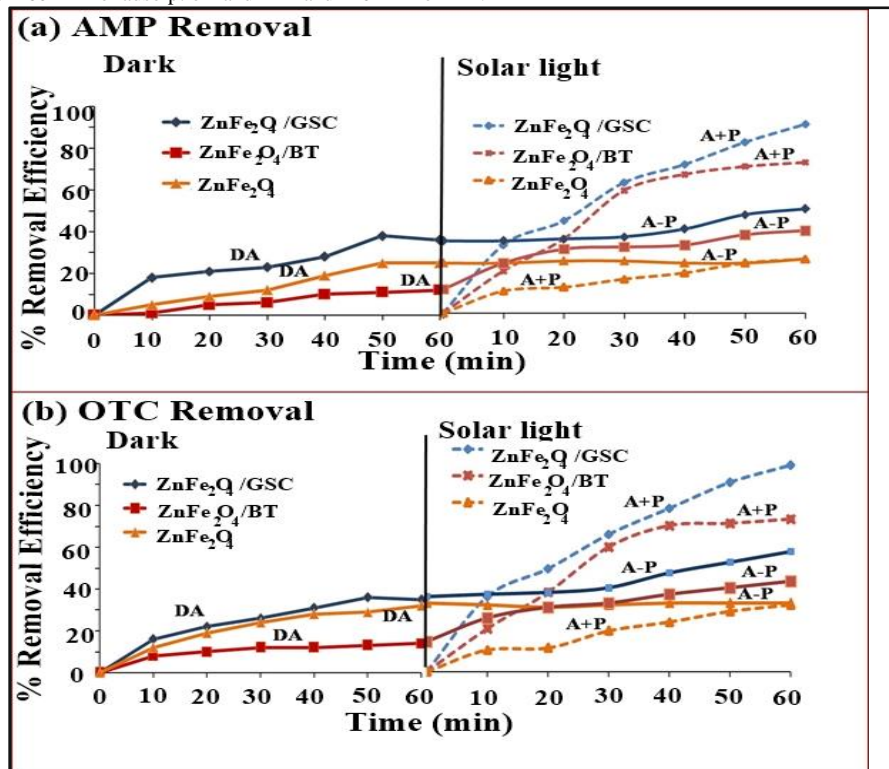
$$\frac{q_t}{dt} = k_2(q_e - q_e)^2 \qquad\qquad (5)$$

$$\frac{t}{q_t} = \frac{1}{k_1 q_e^2} + \frac{t}{q_e} \qquad\qquad (6)$$

where, q_e is the amount of OTC/AMP adsorbed per gram of adsorbent at equilibrium (mg/g), q_t is the amount of adsorbate adsorbed at contact time t(mg/g) and k_2 pseudo second order rate constant (g/mg min). q_e and k_2 can be determined from plot between t/q_t *versus* t.

The kinetic data for ampicillin and oxytetracycline adsorption onto ZnFe₂O₄/BT, ZnFe₂O₄/GSC and ZnFe₂O₄ is given in (**Supplementary Table 1**). The adsorption of AMP and OTC onto ZnFe₂O₄/BT, ZnFe₂O₄/GSC and ZnFe₂O₄ followed pseudo second order knetics. The respective adsorption capacity of ZnFe₂O₄/BT, ZnFe₂O₄/GSC and ZnFe₂O₄ was obtained as 63.01, 58.26 and 16.91 mg/g during AMP adsorption. In case of OTC, the adsorption capacity (q_e) of ZnFe₂O₄/BT, ZnFe₂O₄/GSC and ZnFe₂O₄ was calculated as 64.35, 60.23 and 14.00 mg/g, respectively. The adsorption of liquid phase pollutants onto the surface of catalyst is greatly influenced by initial pH of reaction solution [53, 55].

Below pH of zero point charge, the surface of ZnFe₂O₄/BT and ZnFe₂O₄/GSC and antibiotics are also positively charged and hence the adsorption of antibiotic was very low [56, 57]. At pH 6.0 OTC is found as H₂OTC and HOTC⁻. The ionic species of AMP is mainly existed as HAMP⁻ at near neutral and slightly basic pH range. However, catalyst surface was positively charged below neutral pH thus the negatively charged antibiotics were strongly attracted towards positively charged absorbent molecules [56, 57]. This caused higher adsorption of antibiotics onto adsorbents surface at pH 6 (**Supplementary Table 2**). So, pH 6 is the optimal pH for the OTC and AMP adsorption onto ZnFe₂O₄/GSC and ZnFe₂O₄/BT.

The photodegradation of aqueous phase pollutant is a surface phenomenon as described by Langmuir-Hinshelwood model [58]. Further studies were carried out to find the role of adsorption on photodegradation of OTC and AMP.

Influence of adsorption on photodegradation of antibiotics

The importance of adsorption during photocatalytic degradation by using ZnFe₂O₄/GSC, ZnFe₂O₄/BT and ZnFe₂O₄ was examined under different reaction condition. These conditions includes adsorption in dark (DA), equilibrium adsorption followed by photodegradation (A-P) and simultaneous adsorption and photodegradation process (A+P). **Fig. 4a and b** shows the removal efficiency of ZnFe₂O₄/GSC and ZnFe₂O₄/BT and ZnFe₂O₄ as function of time. The first part of graph indicates adsorption of antibiotics using ZnFe₂O₄/GSC and ZnFe₂O₄/BT and ZnFe₂O₄. 35, 25 and 12 % of AMP removal was observed in dark for ZnFe₂O₄/GSC and ZnFe₂O₄/BT and ZnFe₂O₄, respectively. During OTC removal, 36, 32 and 14 % of efficacy was achieved using ZnFe₂O₄/GSC,   ZnFe₂O₄/BT   and   ZnFe₂O₄, respectively in 60 min.

In case of A-P process, 53, 41 and 26 % of ampicillin removal was observed. While, 56, 42 and

31% of efficiency was attainted in 120 min using $ZnFe_2O_4/GSC$ and $ZnFe_2O_4/BT$ and $ZnFe_2O_4$, respectively. During A-P, saturated adsorption of antibiotics onto catalysts surface slowed down the antibiotic removal. This can be explained by the fact that with the increase in antibiotic concentration the whole surface of catalyst was covered causing the reduction of OH· radicals formation.

In case of simultaneous adsorption and photodegradation (A+P), 92%, 72% and 25 % of ampicillin was removed using $ZnFe_2O_4/GSC$, $ZnFe_2O_4/BT$ and $ZnFe_2O_4$ photocatalyst, respectively. 97%, 74% and 31% of OTC removal efficiency was noted using $ZnFe_2O_4/GSC$ and $ZnFe_2O_4/BT$ and $ZnFe_2O_4$ photocatalyst, respectively in 120 min. During these investigations, A+P process emerged as most efficient process for the degradation of both AMP and OTC.

The kinetics of antibiotic degradation was elucidated by Langmuir-Hinshelwood model (**Eq. 7**) [59, 60]. The experiments were performed under following reaction conditions: catalyst dose = 50 mg/50 ml, OTC concentration = 1×10^{-4} mol dm^{-3}, AMP concentration = 1×10^{-4} mol dm^{-3}, solar light intensity = $35 \times 10^{3} \pm 100$ lx and reaction time = 60 min (AMP) and 120 min (OTC).

$$-\ln\left(\frac{C}{C_0}\right) = kt \qquad (7)$$

where, C_0 and C denotes concentration of antibiotics at the beginning and after time t. the k indicates rate constant. The plots were plotted for AMP and OTC removal process. The linearity of plots ($-\ln(C/C_0)$ and time t) specifies pseudo first order kinetics for photodegradation process. The rate constant for AMP degradation was found to be 2.7×10^{-1} min^{-1} and 2.0×10^{-1} min^{-1} for $ZnFe_2O_4/GSC/A+P$ and $ZnFe_2O_4/BT/A+P$, respectively. For OTC degradation, the respective rate constants were found to be 1.0×10^{-2} min^{-1} and 0.9×10^{-2} min^{-1} under solar light for 120 min using $ZnFe_2O_4/GSC/A+P$ and $ZnFe_2O_4/BT/A+P$.

AMP and OTC mineralization investigations

$ZnFe_2O_4/GSC/A+P$ and $ZnFe_2O_4/BT/A+P$ is considered as combined effect of photocatalytic and adsorption process. The mineralization process involves complete breakdown of antibiotics into CO_2 and respective ions. The COD and CO_2 estimation were executed to explore the degree of OTC and AMP mineralization for hour exposure (**Supplementary Fig. 5a and b**). 99% and 95% of COD was removed using $ZnFe_2O_4/GSC/A+P$ and $ZnFe_2O_4/BT/A+P$ process, respectively. In case of OTC mineralization, 90% and 80% of COD was removal was achieved using $ZnFe_2O_4/GSC/A+P$ and $ZnFe_2O_4/BT/A+P$ process, respectively. The formation of NO_3^-, SO_4^{2-} and CO_2 also confirmed the mineralization of selected antibiotics.

The real degradation process is regarded as combination of photocatalysis and photolysis can be represented as Eq. 8 [60].

$$R = -\frac{dc}{dt} = R_1 + R_2 \qquad (8)$$

where, R, R_1 and R_2 designates net photo degradation, photocatalysis and photolysis rate, respectively. The photolysis had no effect on degradation mineralization. So, photocatalysis was regarded as major process for the degradation.

As the degradation of aqueous phase pollutants is a complex process due to various side reactions besides the main reactions occurring during the degradation of antibiotic. Therefore, to study the kinetics of complex reaction empirical power law model was introduced instead of theoretical models (**Eq. 9**):

$$R = k_1 [ANT]^{n1} \qquad (9)$$

where, k_1 and n_1 are rate constant and order of reaction for photocatalysis, respectively. To find reaction parameters, the differential method of data analysis was applied to **Eq. 9** (**Supplementary Fig. 5c and f**). For AMP mineralization, $ZnFe_2O_4/GSC/A+P$ and $ZnFe_2O_4/BT/A+P$ catalytic systems had rate constants of 6.3×10^{-5} (mol dm^{-3})$^{-0.16}$ h^{-1} and 2.57×10^{-5} (mol dm^{-3})$^{-0.8}$ h^{-1}, respectively (**Supplementary Table 3**). The rate constant for $ZnFe_2O_4/GSC/A+P$ and $ZnFe_2O_4/BT/A+P$ catalytic processes was given by 1.94×10^{-5} (mol dm^{-3})$^{-0.08}$ h^{-1} and 7.4×10^{-6} (mol dm^{-3})$^{-0.97}$ h^{-1}, respectively. The order of reaction more than one signifies complex nature of degradation process. Simple pseudo first order kinetics was not followed during long term degradation process.

During photocatalysis, the charge separation of photo generated electron-hole pairs initiated the various chemical reactions in aqueous phase [61, 59]. The electron and hole subsequently reacted with H_2O and dissolved oxygen to form different oxidizing species. The isopropanol was used as a hydroxyl radical scavenger to explore the role of hydroxyl radical during mineralization process [62]. In the presence of isopropanol, efficiency of process was decreased to 10% and 8% for $ZnFe_2O_4/GSC/A+P$ and $ZnFe_2O_4/BT/A+P$ catalytic systems. While during OTC photodegradation, $ZnFe_2O_4/GSC/A+P$ and $ZnFe_2O_4/BT/A+P$ process had efficiency of 8% and 7% respectively in the presence of isopropanol (2.0×10^{-4} mol dm^{-3}). While holes scavenger NaCl and tertiary butyl alcohol as oxygen scavenger, had no effect on the antibiotic photoremoval [63, 56].

In $ZnFe_2O_4/GSC$ and $ZnFe_2O_4/BT$, both GSC and bentonite possessed surface functionalities for antibiotic adsorption (SiO_2, C=O, O-CH$_3$ [11, 33]. In case of bentonite, Al-OH-Mg and Si-O-Mg functionalities are liable for antibiotics adsorption [44]. Upon irradiation of $ZnFe_2O_4/GSC$ and $ZnFe_2O_4/BT$, the electron-hole pairs were generated [60, 61, 63, 64] (**Fig. 5**). The conduction band electrons reacted with dissolved oxygen to give hydroxyl radicals. The h_{VB}^+ combined with H_2O/OH^- to produce hydroxyl radicals. The hydroxyl radicals

Table 2. Efficiency of photocatalysts with ZnFe2O4 based photocatalysts. The superscript a and b means oxytertacyline and ampicilin respectively.

Photocatalyst	Targeted Pollutant	Irradiation Time (min)	Degradation (%)	Reference
$C_3N_4/ZnFe_2O_4$	Spiramycin	240	95	**[65]**
$ZnFe_2O_4-C_3N_4$	Orange II	240	97	**[66]**
$ZnFe_2O_4/TiO_2$	4- Chlorophenol	120	59.6	**[67]**
$ZnFe_2O_4$/graphene	Methylene blue	90	99	**[68]**
$ZnFe_2O_4$-S1	Rhodamine-B	40	97.5	**[69]**
$ZnFe_2O_4$	Rhodamine-B	150	60	**[70]**
$ZnFe_2O_4$/Ag (22.7%)	Rhodamine-B	150	98	**[70]**
$ZnFe_2O_4$/P25	Rhodamine-B	2.5 h	99.7	**[71]**
$gC_3N_4/Co_{0.5}Zn_{0.5}Fe_2O_4$	Chloromycetin	240	96	**[72]**
$ZnFe_2O4$/GSC	AMP/OTC	120[a]	95	**Present work**
$ZnFe_2O4$/BT	AMP/OTC	120[a]	85	**Present work**
$ZnFe_2O4$/GSC	AMP/OTC	120[b]	98	**Present work**
$ZnFe_2O4$/BT	AMP/OTC	120[b]	91	**Present work**

ultimately mineralized antibiotics in CO_2 and inorganic ions.
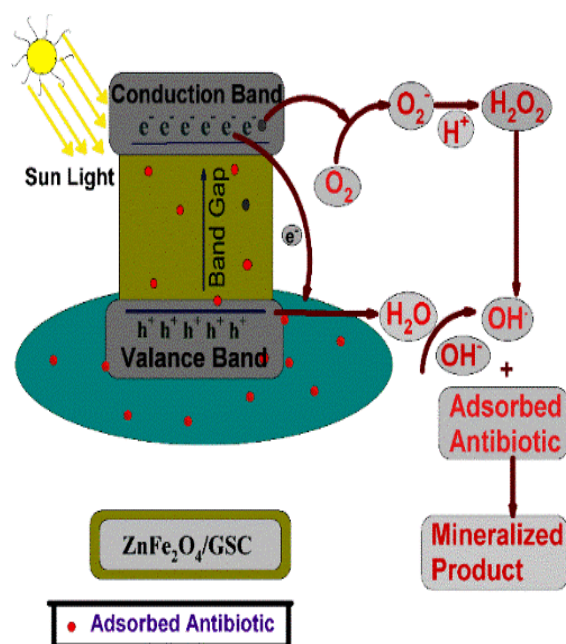
Fig. 5. Mechanistic view of antibiotic mineralization.

The graphene sheet as sink for conduction band electron and reduced the recombination of photo generated electron-hole pair **[11].** The recycle efficacy of both $ZnFe_2O_4$/GSC and $ZnFe_2O_4$/BT was examined for antibiotics removal. The recovery of $ZnFe_2O_4$/GSC and $ZnFe_2O_4$/BT from reaction solution was rapid due to super paramagnetic nature of prepared nanocomposite. Both $ZnFe_2O_4$/GSC and $ZnFe_2O_4$/BT were recovered from reaction mixture using external magnet fields. The removal efficiency of $ZnFe_2O_4$/GSC was found to be 86% for ampicillin removal after 10 catalytic cycles **(Supplementary Fig. 6a)**, whereas removal efficiency of $ZnFe_2O_4$/BT was recorded as 79% **(Supplementary Fig. 6a)**. In case of oxytetracycline removal, both $ZnFe_2O_4$/GSC and $ZnFe_2O_4$/BT had removal efficiency of 88% and 78 %, respectively **(Supplementary Fig. 6b)**.

Conclusion

Magnetically separable $ZnFe_2O_4$/GSC and $ZnFe_2O_4$/BT nanocomposite have been successfully synthesized by modified hydrolysis method with a size of 100 nm and 50 nm, respectively. The various characterization techniques also confirmed the formation of $ZnFe_2O_4$/GSC and $ZnFe_2O_4$/BT. Both $ZnFe_2O_4$/GSC and $ZnFe_2O_4$/BT were applied for the photo removal of ampicillin and oxytetracycline antibiotic from water. The composites were magnetically separated from the reaction mixture in 30 sec and exhibit significant recycle efficiency for ten catalytic cycle. Both $ZnFe_2O_4$/GSC and $ZnFe_2O_4$/BT had significant adsorption capacity for AMP and OTC removal and the antibiotic adsorption followed the pseudo second order kinetics as depicted by power law model. 92% and 72% of AMP and 97% and 74% OTC has been removed in 120 min from aqueous solution by using $ZnFe_2O_4$/GSC and $ZnFe_2O_4$/BT through A+P process. The efficiency of both photocatalysts was compared with existing $ZnFe_2O_4$ based photocatalysts (**Table 2**). $ZnFe_2O_4$/GSC and $ZnFe_2O_4$/BT exhibited significant photocatalytic efficiency for water treatment. Finally, we can conclude that $ZnFe_2O_4$/GSC and $ZnFe_2O_4$/BT nanocomposites based green method can be applied for AMP and OTC degradation in for aqueous pollutants. Due to the magnetic nature of $ZnFe_2O_4$ the nanocomposites can be easily recovered through magnetic separation and therefore can be used as an alternative to treat waste water with high antibiotic concentration under solar light.

Sunil Puri, Dean Academics, Shoolini University, Solan, Himachal Pradesh, India for the constant inspiration during this work.
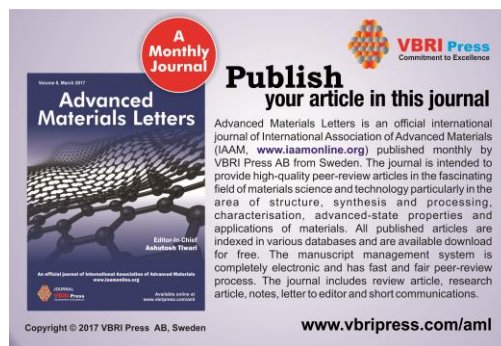
Supporting information

Supporting informations are available from VBRI Press.

References

1. Kummerer, K.; *Chemosphere,* **2009**, *75*, 417.
   DOI: 10.1016/j.chemosphere.2008.11.086
2. Priya, B.; Shandilya, P.; Raizada, P.; Thakur, P.; Singh, N.; Singh, P.; *J. Mol. Catal. A: Chem*., **2016**, *423*, 400.
   DOI: 10.1016/j.envint.2008.07.009
3. Kim, C.H.; Myung, Y.; Cho, Y.J.; Kim, H.S.; Park, S.H.; Park, J.; Kim, J.Y.; Kim, B.; *J. Phys. Chem. C.,* **2009**, *113*, 7085.
   DOI: 10.1021/jp900165c
4. Zhou, Z.; Zhang, Y.; Wang, Z.; Wei, W.; Tang, W.; Shi, J.; Xiong, R.; *Appl. Surf. Sci.,* **2008**, *254*, 6972.
   DOI: 10.1016/j.apsusc.2008.05.067
5. Xuan, S.; Wang, F.; Lai, J.M.Y.; Sham, K.W.Y.; Wang, Y.X.J.; Lee, S.F.; Yu, J.C.; Cheng, C.H.K.; Leung, K.C.F.; *ACS Appl. Mater. Interfaces.,* **2011**, *3*, 237.
   DOI: 10.1021/am1012358
6. Tiwari, A.; Prabaharan, M.; *Journal of Biomaterials Science, Polymer Edition,* **2010**, 21, 937.
   DOI: 10.1163/156856209X452278
7. Jamwal, D.; Kaur, G.; Raizada, P.; Singh, P,; Pathak, D.; Thakur, P; *J Phys Chem C,* **2015**, *119*, 5062.
   DOI: 10.1039/C6RA19818J
8. Priya, B.; Raizada, P.; Singh, N.; Thakur, P.; Singh, P.; *J. Colloid Interface Sci.,* **2016**, *479*, 271.
   DOI: 10.1016/j.jcis.2016.06.067
9. Hankare, P.P.; Patil, R.P.; Jadhav, A.V.; Garadkar, K.M.; Sasikala, R.; *Appl. Catal .B.,* **2011**, *107*, 333.
   DOI: 10.1016/j.apcatb.2011.07.033
10. Li, X.; Hou, Y.; Zhao, Q.; Wang, L.; *J. Colloid Interface Sci.,* **2011**, *358*, 102.
    DOI: 10.1016/j.jcis.2011.02.052
11. Liu, X.; Zheng, H.; Li, Y.; Zhang, W.; *J. Mater. Chem. C.,* **2013**, *1*, 329.
    DOI: 10.1039/C2TC00072E
12. Li, X.; Hou, Y.; Zhao, Q.; Teng, W.; Hu, X.; Chen, G.; *Chemosphere,* **2011**, *82*, 581.
    DOI: 10.1016/j.chemosphere.2010.09.068
13. Rahman, M.M.; Khan, S.B.; Faisal, M.; Asiri, A.M.; Alamry, K.A.; *Sens. Actuators B chem.,* **2012**, *932*, 171.
    DOI: 10.1016/j.snb.2012.06.006
14. The, P.F.; Sharma, Y.; Pramana, S.S.; Srinivasan, M.; *J. Mater. Chem.,* **2011**, *21*, 14999.
    DOI: 10.1039/C1JM12088C
15. Arias, M.; Pantojas, V.M.; Perales, O.; Otano, W.; *J. Magn. Magn. Mater.,* **2011**, *323*, 2109.
    DOI: 10.1016/j.jmmm.2011.02.018
16. Wang, M.; Ai, Z.; Zhang, L.; *J. Phys. Chem. C.,* **2008**, *112*, 13163.
    DOI: 10.1021/jp804009h
17. Deng, Y.; Zhang ,Q.; Tang, S.; Zhang, L.; Deng, S.; Shi, Z.; Chen, G.; *Chem. Commun.,* **2011**, *24*, 6828.
    DOI: 10.1039/C0CC05001F
18. Shen, Y.; Li, X.; Zhao, Q.; Hou, Y.; Tade, M.; Liu, S.; *Mater. Res. Bull.,* **2011**, *46*, 2235.
    DOI: 10.1016/j.materresbull.2011.09.004
19. Song, J.M.; Mao, C.J.; Niu, H.L.; Shen, Y.H.; Zhang, S.Y.; *Cryst. Eng. Comm.,* **2010**, *12*, 3875.
    DOI: 10.1039/C003497P
20. Li, T.B.; Chen, G.; Zhou, C.; Shen, Z.Y.; Jin, R.C.; Sun, J.X.; *Dalton. Trans.,* **2011**, *40*, 6751.
    DOI: 10.1039/C1DT10471C
21. Xu, Y.; Schoonen, M.A.A.; *Am. Mineral.,* **2000**, *85*, 543.
    DOI: 10.2138/am-2000-0416
22. Hameed, A.; Montini, T.; Gombac, V.; Fornasiero, P.; *J. Am. Chem. Soc.,* **2008**, *130*, 9658.
    DOI: 10.1021/ja803603y
23. Chai, S.Y.; Kim, Y.J.; Jung, M.H.; Chakraborty, A.K.; Jung, D.; Lee, W.I.; *J. Catal.,* **2009**, *262*, 144.
    DOI: 10.1016/j.jcat.2008.12.020
24. Shan, Z.; Wang, W.; Lin, X.; Ding, H.; Haung, F.; *J. Solid State Chem.,* **2008**, *181*, 1361.
    DOI: 10.1016/j.jssc.2008.03.001
25. Gautam, S.; Shandilya, P.; Priya, B.; Singh, V.P.; Raizada, P.; Rai, Radheshyam.; Valente, M.A.; Singh, P.; *Sep. Purif. Technol*., **2017**, *172*, 498.
    DOI: 10.1016/j.seppur.2016.09.006
26. Luckham, P.F.; Rossi, S.; *Adv. Colloid Interfac.,* **1999**, *82*, 43.
    DOI: 10.1016/S0001-8686(99)00005-6
27. Eren, E.; Afsin, B.; *J. Hazard Mater.,* **2008**, *151*, 682.
    DOI: 10.1016/j.jhazmat.2007.06.040
28. Ghiaci, M.; Sedaghat, M.E.; Aghaei, H.; Gil, A.; *J. Chem. Technol. Biotechnol.,* **2009**, *84*, 1908.
    DOI: 10.1002/jctb.2264
29. Yao, W.; Zhang, B.; Huang, C.; Ma, C.; Song, X.; Xu, Q.; *J. Mater. Chem.,* **2012**, *22*, 4050.
    DOI: 10.1039/C2JM14410G
30. Zhang, Y.J.; Liu, L.C.; Chen, D.P.; *Powder Technol.,* **2013**, *241*, 7.
    DOI: 10.1016/j.powtec.2013.02.031
31. Li, Y.P.; Zhan, J.; Huang, L.Y.; Xu, H.; Li, H.M.; Zhang, R.X.; Wu, S.L.; *RSC Adv.,* **2014**, *4*, 11831.
    DOI: 10.1039/C3RA46818F
32. Raizda, P.; Gautam S.; Priya, B.; Singh, P**.;** *Adv. Mater. Lett.,* **2016**, 4, 312.
    DOI: 10.5185/amlett.2016.5847
33. Gupta, S.S.; Sreenivasan, S.T.; Mundampra, M.S.; Kumar, D.S.; Thalappil, P.; *ACS Appl. Mater Interfaces.,* **2012**, *8*, 4156.
    DOI: 10.1021/am300889u
34. Guoli, F.; Zhijun, G.; Lan, Y.; Feng, L.; *Chem. Eng. J.,* **2009**, *155*, 534.
    DOI: 10.1016/j.cej.2009.08.008
35. Pare, B.; Singh, P.; Jonnalagadda, S.B.; *Ind. J. Chem. Tech.,* **2010**, *17*, 391.
36. Dubey, R.; Bajpai, J.; Bajpai, A.K.; *J. Water Proc. Eng.,* **2015**, *5*, 83.
    DOI: 10.1016/j.jwpe.2015.01.004
37. McAllister, M.J.; Li, J.L.; Adamson, D.H.; Schniepp, H.C.; Abdala, A.A.; Liu, J.; Alonso, M.H.; Milius, D.L.; Car, R.; Purdhomme, R.K.; Aksay, I.A.; *Chem. Mater.,* **2007**, *19*, 4396.
    DOI: 10.1021/cm0630800
38. Yeh, T.F.; Syu, J.M.; Cheng, C.; Chang, T.H.; Temg, H.; *Adv. Funct. Mater.,* **2010**, *14*, 2255.
    DOI: 10.1002/adfm.201000274
39. Xu, Y.X.; Bai, H.; Lu, G.W.; Li, C.; Shi, G.Q.; *J. Am. Chem. Soc.,* **2008**, *130*, 5856.
    DOI: 10.1021/ja800745y
40. Wu, J.L.; Bai, S.; Shen, X.P.; Jiang, L.; *Appl. Surf. Sci.,* **2010**, *257*, 747.
    DOI: 10.1016/j.apsusc.2010.07.058
41. Tewari, C.J.; Kamal, M.; *Int. J. Food Sci. Technol.,* **2007**, 42, 200.
    DOI: 10.1111/j.1365-2621.2006.01209
42. Sathyal, P.; Velraj, G.; Meyvel, S.; *Adv. Appl. Sci. Res.,* **2012**, 2, 776.
    ISSN: 0976-8610
43. Anchieta, C.G.; Cancelier, A.; Mazutti, M.A.; Jahn, S.L.; Kuhn, R.C.; Gündel, A.; Filho, O.C.; Foletto, E.L.; *Mater.,* **2014**, *7*, 6281.
    DOI: 10.3390/ma7096281
44. Alabarse, F.G.; Conceição, R.V.; Balzaretti, N.M.; Schenato, F.; Xavier, A.M.; *Appl. Clay Sci.,* **2011**, *1*, 202.
    DOI: 10.1016/j.clay.2010.11.017
45. Natkanski, P.; Bialas, A.; Kustrowski, P.; *Chemik.,* **2012**, *7*, 742.
    ICID: 1003299
46. Parker, R.W.; Frost, R.L.; *Clays Clay Miner.,* **1996**, *44*, 32.
47. Kalaleh, H.A.; Tally, M.; Atassi, Y.; *Res. Rev. Polym.,* **2013**, 4, 145.
48. Cui, H.J.; Shi, J.W.; Yuan, B.; Fu, M.L.; *J. Mater. Chem. A.,* **2013**, *1*, 5902.
    DOI: 10.1039/C3TA01692G

49. Akhavan, O.; Abdolahad, M.; Esfandiar, A.; Mohatashamifar, M.; *J. Phys. Chem. C.,* **2010,** *114*, 12955.
    DOI: 10.1021/jp103472c
50. Xiao, Y.; Zai, J.; Tao, L.; Li, B.; Han, Q.; Yu, C.; Qian, X.; *Phys. Chem. Chem. Phys.,* **2013,** *15*, 3939.
    DOI: 10.1039/C3CP50220A
51. Frost, R.L.; Rintoul, L.; *Appl. Clay. Sci.,* **1996,** *11*, 171.
    DOI: 10.1016/S0169-1317(96)00017-8
52. Cui, H.J.; Shi, J.W.; Yuan, B.; Fu, M.L.; *J. Mater. Chem. A.,* **2013,** *1*, 5902.
    DOI: 10.1039/C3TA01692G
53. Gupta, V.K.; Pathania, D.; Sharma, S.; Singh, P.; *J. Colloid. Interface Sci.,* **2013,** *401*, 125.
    DOI: 10.1016/j.jcis.2013.03.020
54. Singh, P.; Raizada, P.; Pathania, D.; Sharma, G.; Sharma, P.; *Indian J. Chem. Technol.,* **2013,** *20*, 305.
    ISSN: 0975-0991
55. Yadav, S.; Srivastava, V.; Banerjee, S.; Weng, C.H.; Sharma, Y.C.; *Catena.,* **2013,** *100*, 120.
    DOI: 10.1016/j.catena.2012.08.002
56. Zhao, C.; Pelaez, M.; Duan, X.; Deng, H.; OShea, K.; Fatta-Kassinos, D.; Dionysiou, D.D.; *App. Catal. B Environ.,* **2013,** *83*, 134,
    DOI: 10.1016/j.apcatb.2013.01.003
57. Gautam, S. Shandilya P , Singh V. P. , Raizada P. Singh, P. J. Water Process Eng. **2016** (In press).
    DOI: 10.1016/j.jwpe.2016.10.008
58. Dimitrakopoulou, D.; Rethemiotaki, I.; Frontistis, Z.; Xekoukoulotakis, N.P.; Venieri, D.; Mantzavinos, D.; *J. Environ. Manage.,* **2012,** *98*, 168.
    DOI: 10.1016/j.jenvman.2012.01.010
59. Pare, B.; Singh, P.; Jonnalgadda, S.B.; *Indian J. Chem. Sect. A.;* **2008,** *47*, 830.
    ISSN: 0975-0975
60. Saien, J.; Ardjmand, R.R.; Iloukhani, H.; *Phys. Chem. Liq.,* **2003,** *41*, 519.
    DOI: 10.1080/00319100310001604849
61. Kansal, S.K.; Singh, M.; Sud, D.*; J. Hazard. Mater.,* **2007,** *141*, 581.
    DOI: 10.1016/j.jhazmat.2006.07.035
62. Buxton, G.V.; Greenstock, C.; Hellman, W.P.; Ross, A.B.; *J. Phys. Chem.,* 1**1988,** *7*, 513.
    DOI: 10.1063/1.555805
63. Pare, B.; Jonnalagadda, S.B.; Tomar, H.; Singh, P.; Bhagwat, V.W.; *Desalination,* **2008,** *232*, 80.
    DOI: 10.1016/j.desal.2008.01.007
64. Raizada, P.; Singh, P.; Kumar, A.; Sharma, G.; Pare, B.; Jonnalagadda, S.B.; Thakur, P.; *Appl. Catal. A.,* **2014,** *486,* 159.
    DOI: 10.1016/j.apcata.2014.08.043
65. Chen, L.; Ma, W.; Dai, J.; Zhao, J.; Li, C.; Yan, Y.; *J. Photochem. Photobiol.,* A **2016**, *328*, 24.
    DOI: 10.1016/j.jphotochem.2016.04.026
66. Yao, Y.; Cai, Y.; Lu, F.; Qin, J.; Wei, F.; Xu, C.; Wang, S.; *Ind. Eng. Chem. Res*., **2014**, *53*, 17294.
    DOI: 10.1021/ie503437z
67. Hou, Y.; Li, X.; Zhao, Q.; Quan, X.; Chen, G.; *Environ. Sci. Technol.*, **2010**, *44*, 5098.
    DOI: 10.1021/es100004u
68. Fu, Y.; Wang, X.; Ind. Eng. *Chem. Res.,* **2011,** *50*, 7210.
    DOI: 10.1021/ie200162a
69. Han, L.; Zhou, X.; Wan, L.; Deng, Y.; Zhan, S.*; J. Environ. Chem. Eng*., **2014**, *2*, 123.
    DOI: 10.1016/j.jece.2013.11.031
70. Cao, X.; Gu, L.; Lan, X.; Zhao, C.; Yao, D.; Sheng, W.; *Mater. Chem. Phys*., **2007**, *106*,175.
    DOI: 10.1016/j.matchemphys.2007.05.033
71. Zhang, G.Y.; Ya-Qiu Sun, Y.Q.; Gao, D.Z.; Xu, Y.Y.; *Mater. Res. Bull*., **2010**, *45*, 755.
    DOI: 10.1016/j.materresbull.2010.03.025
72. Ma, W.; Chen, L.; Dai, J.; Lib, C.; Yan, Y.; *RSC Adv*., **2016**, 1.
    DOI: 10.1039/C6RA07915F

Supporting Information

Fig. S1. (a) TEM image of ZnFe$_2$O$_4$/GSC, (b) TEM image of ZnFe$_2$O$_4$/BT, (c) magnified TEM image of selected area from Fig. 2 (a) , (d) magnified TEM image of selected area from Fig. 2(b) , (e) SAED pattern of ZnFe$_2$O$_4$/GSC and (f) SAED pattern of ZnFe$_2$O$_4$/BT.
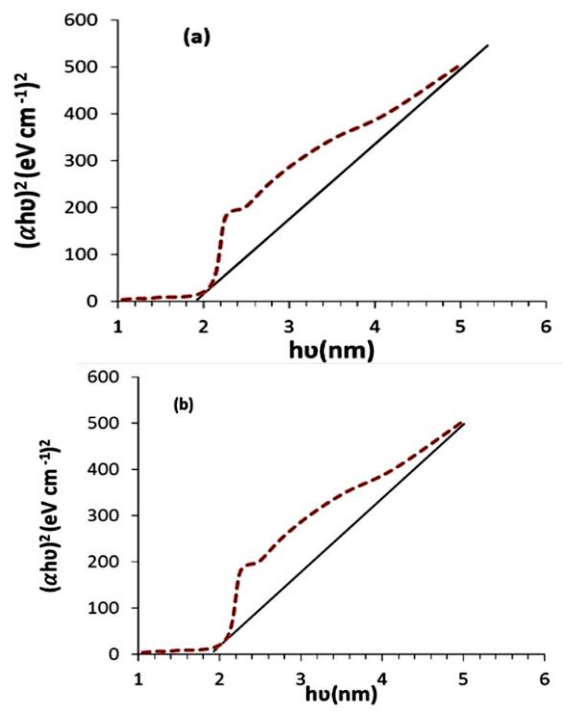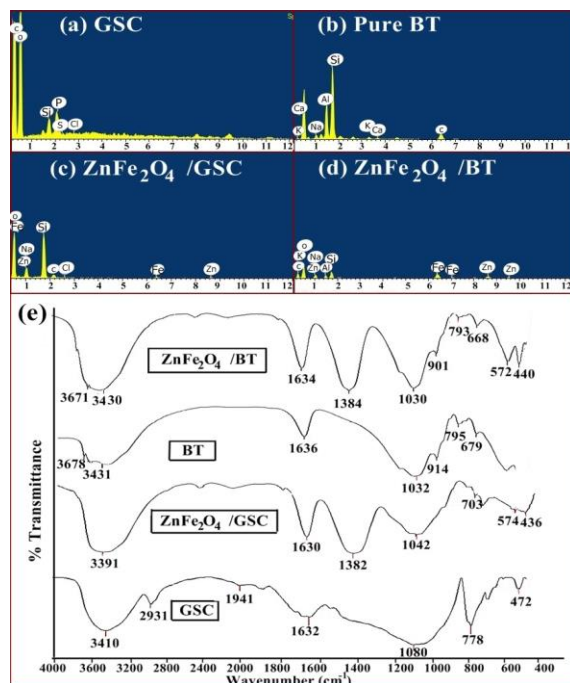

Fig. S2. (a) EDX spectrum of GSC, (b) EDX sperum of BT, (c) EDX spectrum of ZnFe$_2$O$_4$/GSC, (d) EDX spectrum of ZnFe$_2$O$_4$/BT, (e) FTIR spectra of native GSC, ZnFe$_2$O$_4$/GSC, BT and ZnFe$_2$O$_4$/BT.

Supplementary Figure S3: Band gap analysis of (a) ZnFe$_2$O$_4$/GSC and (b) ZnFe$_2$O$_4$/BT.
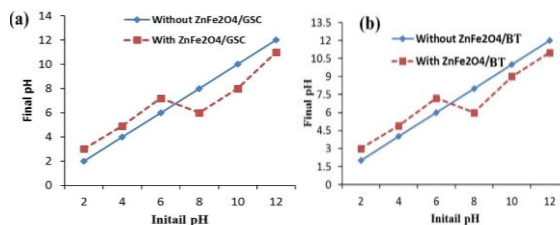
Fig. S4. pH$_{ZPC}$ analysis of (a) ZnFe$_2$O$_4$/GSC and (b) ZnFe$_2$O$_4$/BT.
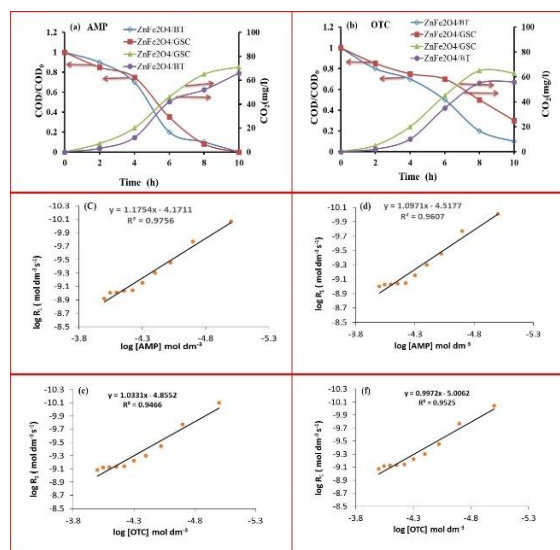

Fig. S5. Mineralization kinetics of OTC and AMP. COD and CO$_2$ measurements during mineralization of AMP (a) and of OTC (b).The variation of AMP mineralization rate versus its concentration using (c) ZnFe$_2$O$_4$/GSC and (d) ZnFe$_2$O$_4$/BT. The variation of OTC mineralization rate versus its concentration using (e) ZnFe$_2$O$_4$/GSC and (f) ZnFe$_2$O$_4$/BT. Reaction parameter: [catalyst] = 50 mg/100ml ; pH= 6.0; Solar light intensity = 35 × 10^3 ± 10, 000 lx; reaction time = 10 h

Fig. S6. Recycle efficiency of $ZnFe_2O_4$/BT and $ZnFe_2O_4$/GSC (a) for AMP degradation, (b) for OTC degradation. Reaction coditions [AMP] = 1×10^{-4} mol dm^{-3}; [OTC]= 1×10^{-4} mol dm^{-3}; [catalyst] = 50 mg/100ml; initial reaction pH= 6.0; solar light intensity= $35 \times 10^3 \pm 1000$ lx.

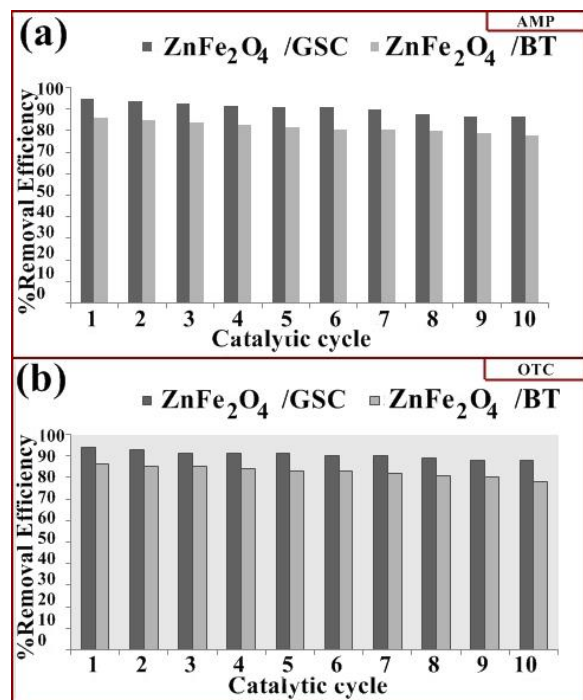**Table 3.** Kinetic parameters for long term degradation of OTC and AMP. Reaction parameter: [catalyst] = 50 mg/100 mL; pH= 6.0; Solar light intensity = $35 \times 103 \pm 1000$ lx; reaction time = 10 h.

The superscript "a" means AMP and "b" means OTC.

Parameters	ZnFe₂O₄/GSC/A+P	ZnFe₂O₄/BT/A+P
$^a n_1$	1.17	1.09
$^a k_1$	$6.3 \times 10^{-5} (mol\ dm^{-3})^{-0.16}\ h^{-1}$	$2.57 \times 10^{-5}\ (mol\ dm^{-3})^{-0.8}\ h^{-1}$
$^a R$	6.3×10^{-5} [AMP]$^{1.16}$ mol $dm^{-3}\ h^{-1}$	2.57×10^{-5} [AMP]$^{1.08}$ mol $dm^{-3}\ h^{-1}$
$^b n_1$	1.08	1.97
$^b k_1$	$1.94 \times 10^{-5}\ (mol\ dm^{-3})^{-0.08}\ h^{-1}$	$7.4 \times 10^{-6}\ (mol\ dm^{-3})^{-0.97}\ h^{-1}$
$^b R$	1.94×10^{-05} [OTC]$^{1.07}$ mol $dm^{-3}\ h^{-1}$	7.4×10^{-6} [OTC]$^{1.97}$ mol $dm^{-3}\ h^{-1}$

Table 1. Adsorption kinetics for OTC and AMP adsorption onto $ZnFe_2O_4$/BT and $ZnFe_2O_4$/GSC. Reaction condition [AMP] = $1\times1\ 0^{-4}$ mol dm^{-3}; [OTC] = 1×10^{-4} mol dm^{-3}; [catalyst] = 50 mg/100 ml; pH= 6.0; reaction time = 120 min.

	Pseudo first order kinetics					
	$k_1(min^{-1})$		$q_e(mg/g)$		R^2	
	AMP	OTC	AMP	OTC	AMP	OTC
$ZnFe_2O_4$/GSC	0.017	0.015	56.35	56.73	0.92	0.92
$ZnFe_2O_4$/BT	0.015	0.014	53.56	52.00	0.91	0.91
$ZnFe_2O_4$	0.007	0.006	11.12	10.56	0.90	0.86
	Pseudo second order kinetics					
	$k_2(g/(mg\ min)$		$q_e(mg/g)$		R^2	
	AMP	OTC	AMP	OTC	AMP	OTC
$ZnFe_2O_4$/GSC	0.00016	0.00015	63.01	64.35	0.98	0.98
$ZnFe_2O_4$/BT	0.0011	0.00016	58.26	60.23	0.97	0.96
$ZnFe_2O_4$	0.00007	0.00009	16.91	14.00	0.96	0.98

Table 2. Effect of pH on antibiotics adsorption. Reaction condition: [AMP]= 1×10^{-4} mol dm^{-3}; [OTC] = 1×10^{-4} mol dm^{-3}; [catalyst] = 50 mg/100 ml; pH= 6.0; reaction time = 120 min.

	AMP				OTC			
Initial pH	ZnFe₂O₄/BT		ZnFe₂O₄/GSC		ZnFe₂O₄/BT		ZnFe₂O₄/GSC	
	q_e	Final pH	q_e	Final pH	q_e	Final pH	q_e	Final pH
2.0	14	1.9	16	1.9	21	1.9	12	1.8
4.0	22	2.5	20	3.7	45	2.7	37	3.5
6.0	60	5.7	60	6.2	64	5.5	63	5.9
8.0	38	7.2	34	6.6	47	6.9	22	6.9
10.0	17	9.2	16	8.8	22	8.5	9	8.1